Descriptor-tensor texture analysis of myostatin-edited rabbit muscle: a two-study replication

Ștefan Țălu

The Directorate of Research, Development and Innovation Management (DMCDI), The Technical University of Cluj-Napoca, Cluj-Napoca, Romania. Corresponding author: Ş. Ţălu, stefan.talu@auto.utcluj.ro

https://doi.org/10.67784/0097

Abstract. Loss-of-function mutations of the myostatin gene (*MSTN*) produce the double-muscle phenotype in several mammals, and CRISPR/Cas9 editing has reproduced it in the domestic rabbit (*Oryctolagus cuniculus*). Histological evidence for the phenotype is usually reported as fibre counts and diameters, which discard the spatial organisation of the tissue. Here, a hierarchical texture-descriptor tensor $D[m,k,l,r]$ (10 channels × 4 Gaussian scales × 4 orientations × 1 or 4 regions of interest, ROI) was applied to open-access haematoxylin-eosin (H&E) sections from two independent CRISPR/Cas9 studies: nine *gluteus maximus* panels of wild-type (WT), heterozygous (*MSTN*+/−) and homozygous (*MSTN*−/−) rabbits at 10×, 20× and 40× (discovery set), and *gluteus maximus* and tongue panels of WT and *MSTN*+/− rabbits calibrated at 0.595 µm/px (replication set). Anisotropy A and texture axis ψ were derived from the structure matrix, with block-bootstrap 95% confidence intervals and isotropic Fourier-phase surrogates. All 13 sections were significantly anisotropic relative to the surrogate floor ($P \leq 0.035$). In the discovery set the *MSTN*−/− muscle was the most isotropic (A = 0.06-0.14 vs 0.33-0.46 at s = 2 px), but this did not replicate: in the replication set the WT *gluteus* was nearly isotropic (A = 0.029) and the *MSTN*+/− *gluteus* anisotropic (A = 0.214). Across all studies, A tracked the orientational order of the segmented fibre profiles (Spearman ρ = 0.78, P = 0.013), showing that it measures section and packing geometry rather than genotype. In contrast, the co-occurrence signature replicated: in all eight edited-versus-WT comparisons the GLCM contrast was lower (−6% to −30%; block-bootstrap 95% CI excluding zero in 7/8) and the homogeneity higher (+0.5% to +9%; 6/8), and the derivative kurtosis was higher in 7/8. The edited *gluteus* showed larger fibres in both studies (mean area 943 vs 438 µm² in the replication set). The GLCM contrast-homogeneity pair is therefore proposed as a candidate, segmentation-free texture signature of *MSTN* disruption, pending validation on independent animals, for rabbit genetics and breeding studies, whereas anisotropy should be interpreted as a geometric covariate.
Keywords: rabbit, myostatin, double muscling, CRISPR/Cas9, histology, texture analysis, structure tensor, anisotropy.

Introduction. Myostatin (growth/differentiation factor 8, GDF-8) is a member of the TGF-β superfamily that acts as a negative regulator of skeletal muscle mass (McPherron et al., 1997; Lee, 2004). Natural loss-of-function alleles cause the double-muscled phenotype of Belgian Blue and Piedmontese cattle (Grobet et al., 1997; Kambadur et al., 1997), the 'bully' whippet (Mosher et al., 2007) and gross muscle hypertrophy in a human child (Schuelke et al., 2004). Because the rabbit is both a meat species and a laboratory model, *MSTN* has been one of the first targets of genome editing in *Oryctolagus cuniculus*: CRISPR/Cas9 knockouts increased body weight and muscle mass, with hypertrophy and/or hyperplasia of the myofibres (Guo et al., 2016; Lv et al., 2016; Zheng et al., 2022).

Genetic analyses of coat colour, albinism and breed structure have a long tradition in Rabbit Genetics (Proorocu et al., 2019; Păpuc & Petrescu-Mag, 2021; Proorocu & Kovacs, 2022), but quantitative image-based phenotyping of muscle is less common. Histological evaluation of the *MSTN* phenotype is usually restricted to fibre counts, cross-sectional areas or diameters, obtained manually or with semi-automatic tools (Smith & Barton, 2014; Bankhead et al., 2017). These metrics ignore how fibres are packed and oriented, although the arrangement of fibres and connective septa is exactly what changes when muscle grows by hyperplasia rather than by hypertrophy.

Texture analysis offers a complementary description that uses every pixel of the section (Haralick et al., 1973; Ţălu, 2012). The present author has previously applied multiscale, stereometric and fractal descriptors to biological and engineered surfaces (Ţălu et al., 2016; Garczyk et al., 2017; Conceição et al., 2021; Ţălu et al., 2021) and has proposed integrative multidimensional frameworks for translational human and veterinary medicine (Ţălu, 2026a, 2026b) and for aquaculture (Petrescu-Mag et al., 2026). Building on these works, a hierarchical descriptor tensor was defined that organises ten gradient, curvature, co-occurrence and autocorrelation channels by scale, orientation and region, and reduces them to an anisotropy index A and a texture axis ψ through the structure matrix (Bigun & Granlund, 1987; Ţălu, 2027a). The same tensor has been applied to guppy and porcine muscle and to soil thin sections (Ţălu, 2026c, 2027b, 2027c).

The aims of this study were (i) to test whether the descriptor tensor discriminates the three *MSTN* genotypes in published, open-access H&E sections of rabbit *gluteus maximus*, (ii) to test the robustness of the result to magnification and its agreement with fibre-level morphometry, and (iii) to check which descriptors replicate in an independent CRISPR/Cas9 rabbit study with a different laboratory, staining protocol and imaging system.

Material and Method

Source images. The nine H&E photomicrographs of Figure 7B in Zheng et al. (2022), published in Frontiers in Veterinary Science under the Creative Commons Attribution (CC BY) licence, were used without any further animal experimentation. They show transverse sections (5 µm, 4% paraformaldehyde fixation) of *gluteus maximus* from WT, *MSTN*+/− and *MSTN*−/− rabbits generated with CRISPR/Cas9, each photographed at 10×, 20× and 40× (Zheng et al., 2022). The published figure (1520 × 2480 px, RGB) was cropped into nine panels of 301-306 × 253-256 px. The yellow scale bars, whose numerical values are not legible, were removed by fast-marching inpainting (Telea, 2004); they occupied 0.2-2.6% of the analysed area. The bars had the same length in pixels (60-62 px) within each magnification, so the three genotypes are on a common pixel scale within a row of the figure. All results are therefore given in pixels and compared within magnification (Figure 1).

Descriptor tensor. Each panel was converted to luminance $Y = 0.299R + 0.587G + 0.114B$ and standardised to zero mean and unit variance. Gaussian scale-space derivatives were computed at $s \in \{1, 2, 4, 8\}$ px, and directional first and second derivatives at $\theta \in \{0, \pi/4, \pi/2, 3\pi/4\}$ (Figure 2). For every scale k, orientation l and region r, ten channels were evaluated: D1 mean $|\partial G|$, D2 mean $(\partial G)^2$, D3 kurtosis and D4 Shannon entropy of the directional derivative, D5 mean $|\partial^2 G|$, D6-D9 contrast, homogeneity, energy and correlation of a symmetric 16-level grey-level co-occurrence matrix with displacement s along θ (Haralick et al., 1973), and D10 the normalised autocorrelation at lag $2s$. The result is the tensor $D[m,k,l,r]$ with $10 \times 4 \times 4 \times R$ elements, $R = 1$ (whole panel minus a 12 px margin, about 6.4×10^4 px) or $R = 4$ (quadrants).

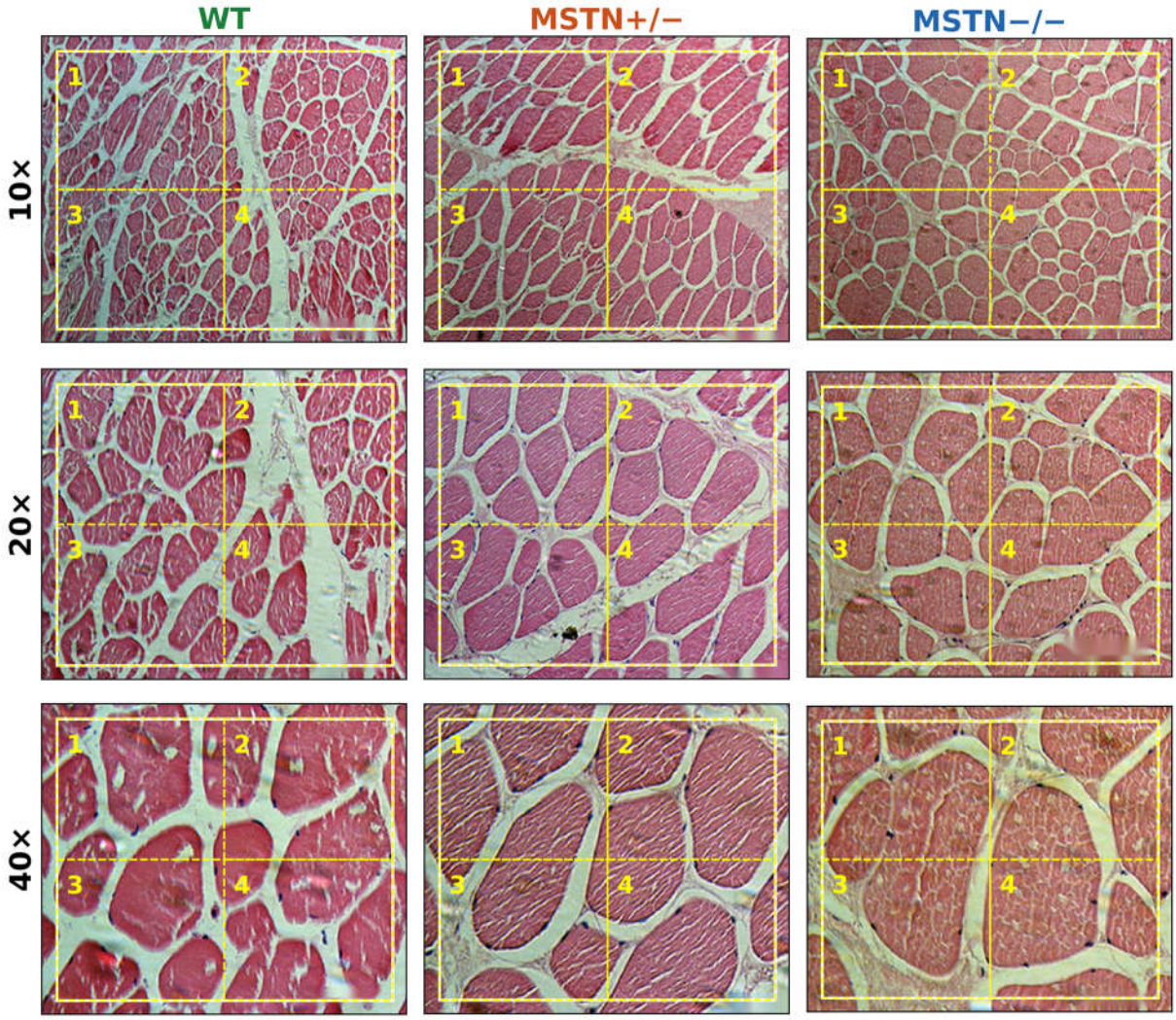


Figure 1. H&E cross-sections of rabbit *gluteus maximus* analysed in this study (WT, *MSTN*+/− and *MSTN*−/−; rows 10×, 20×, 40×). White frame: ROI = 1 (margin 12 px); yellow dashed frames: the four quadrants (ROI = 4). Images cropped from Zheng et al. (2022), Figure 7B, CC BY; scale bars inpainted for analysis.

Anisotropy and axis. From D2 the structure matrix was assembled as $J_{xx} = \mathrm{D2}(0)$, $J_{yy} = \mathrm{D2}(\pi/2)$, $J_{xy} = 1/2\,[\mathrm{D2}(\pi/4) - \mathrm{D2}(3\pi/4)]$, and the anisotropy index $A = 2\sqrt{\left((J_{xx} - J_{yy})/2\right)^2 + J_{xy}^2}\Big/\left(J_{xx} + J_{yy}\right) \in [0, 1]$ and texture axis $\psi = 1/2\,\mathrm{atan2}\left(2J_{xy}, J_{xx} - J_{yy}\right) + 90°\ (\mathrm{mod}\ 180°)$ were obtained (Bigun & Granlund, 1987). The energy identity D2(0) + D2(π/2) = D2(π/4) + D2(3π/4) was verified to machine precision. Uncertainty was estimated by a moving-block bootstrap (8 × 8 blocks, 1000 resamples; Künsch, 1989), and the null hypothesis of isotropy by 200 surrogates with the radially averaged Fourier amplitude of each panel and random phases (Theiler et al., 1992); *P* is the fraction of surrogates with *A* at least as large as observed. For ROI = 4 the pooling inequality (Țălu, 2027a) $A(\cup r) \le \Sigma E_r A_r / \Sigma E_r$, with $E_r = \mathrm{tr}\, J_r$, was checked. As an independent estimator, a Gaussian-windowed structure-tensor field (*s* = 2 px, *ρ* = 16 px) gave the mean local coherence $\overline{\kappa}$ and the energy-weighted resultant *R* of the doubled local axes (Rezakhaniha et al., 2012). The characteristic scale s^* was taken as the maximum of s^2 tr $J(s)$ over nine log-spaced scales (Lindeberg, 1998). Spearman correlations between channels were computed over the 64 scale × orientation × quadrant entries of all three genotypes.

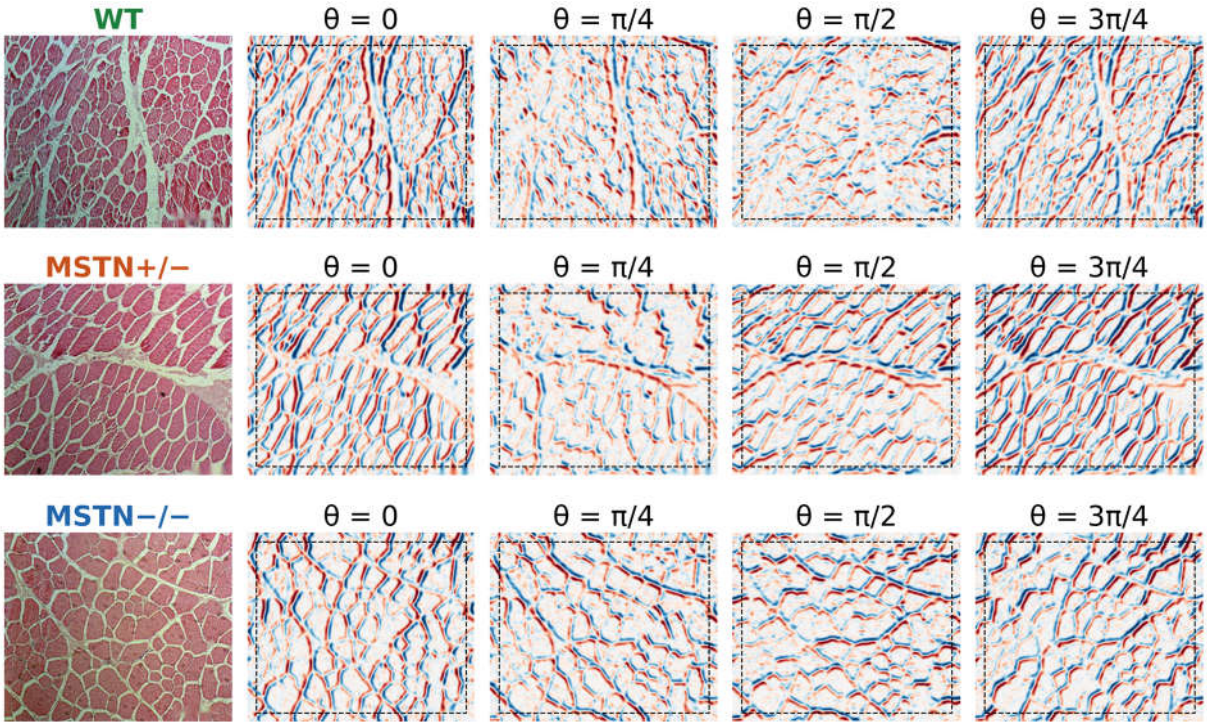


Figure 2. First-order Gaussian directional derivatives (s = 2 px) at the four orientations for the 10× panels; red and blue denote positive and negative responses, the dashed frame marks ROI = 1.

Fibre morphometry. For an independent check, fibres were segmented on the CIELAB a^* (red-green) channel with Otsu thresholding (Otsu, 1979), morphological closing and hole filling, followed by marker-controlled watershed on the distance transform (h-maxima markers; van der Walt et al., 2014). For each fibre not touching the panel border, the area (px²), circularity $4\pi A/P^2$ and orientation of the major axis were measured; the orientational order of fibre profiles, Rshape, was defined as the area- and elongation-weighted resultant of the doubled major-axis angles. Fibre density was expressed per 10^4 px². At 40× only 12-16 complete fibres per panel were available, so morphometry is reported mainly at 10× and 20×.

Software. All computations were made in Python 3 with NumPy, SciPy, OpenCV and scikit-image; the analysis is fully reproducible from the published figure, with a fixed random seed (seed = 1).

Replication set. Figure 5A of Lv et al. (2016), published in Scientific Reports under the Creative Commons Attribution 4.0 licence, shows H&E sections of *gluteus maximus* (cross-section) and tongue (mixed cross and longitudinal sections) from WT and *MSTN*+/− F1 rabbits at 2 months of age (4% paraformaldehyde, paraffin embedding, Nikon TS100 microscope; Lv et al., 2016). The figure (1575 × 2309 px) was cropped into four panels of 684 × 512 px. The printed 50 µm scale bars measured 84 px in all four panels, giving a calibration of 0.595 µm/px (s = 2 px ≈ 1.19 µm); the bars and labels were inpainted (1.3% of the analysed area). The same tensor, bootstrap and surrogate settings were used with a 16 px margin. Fibres of the *gluteus* panels were segmented as above (closing and opening of 2 iterations, h-maxima height 4 px, minimum area 60 px²) and measured in µm². Tongue panels, which contain longitudinally cut fibres, were analysed with the tensor only.

Replication statistics. For the distribution-shape and co-occurrence channels (D3, D4, D6, D7) at s = 2 px, each ROI was divided into 6 × 6 blocks, the orientation-averaged channels were computed per block, and 1000 block-bootstrap resamples gave 95% CIs for the percentage change of each edited panel relative to the WT panel of the same study, tissue and magnification. Eight such comparisons were available (*MSTN*+/− and

MSTN−/− at three magnifications in the discovery set; *MSTN*+/− *gluteus* and tongue in the replication set). Because the discovery comparisons share WT panels, consistency across comparisons is reported descriptively.

Results and Discussion

Descriptor tensor. The full tensor for ROI = 1 at 10× is shown in Figure 3. Gradient and curvature channels (D1, D2, D5) decreased by about one decade per octave of scale in all genotypes, as expected for smooth stained tissue, and were nearly equal between genotypes once the luminance had been standardised (Table 1). The genotype differences were concentrated in the distribution-shape and co-occurrence channels. From WT through *MSTN*+/− to *MSTN*−/−, the kurtosis D3 increased (3.88, 4.27, 4.52), the entropy D4 decreased (3.99, 3.91, 3.87 bits), the GLCM contrast D6 decreased (1.14, 1.01, 0.79), and the homogeneity D7, energy D8, correlation D9 and autocorrelation D10 increased. This monotonic gene-dose ordering indicates a smoother, more homogeneous intrafibre texture with sparser, sharper septa in the knockout, consistent with larger fibres occupying more of the field (fibre area fraction 0.60, 0.59 and 0.72; Table 4).

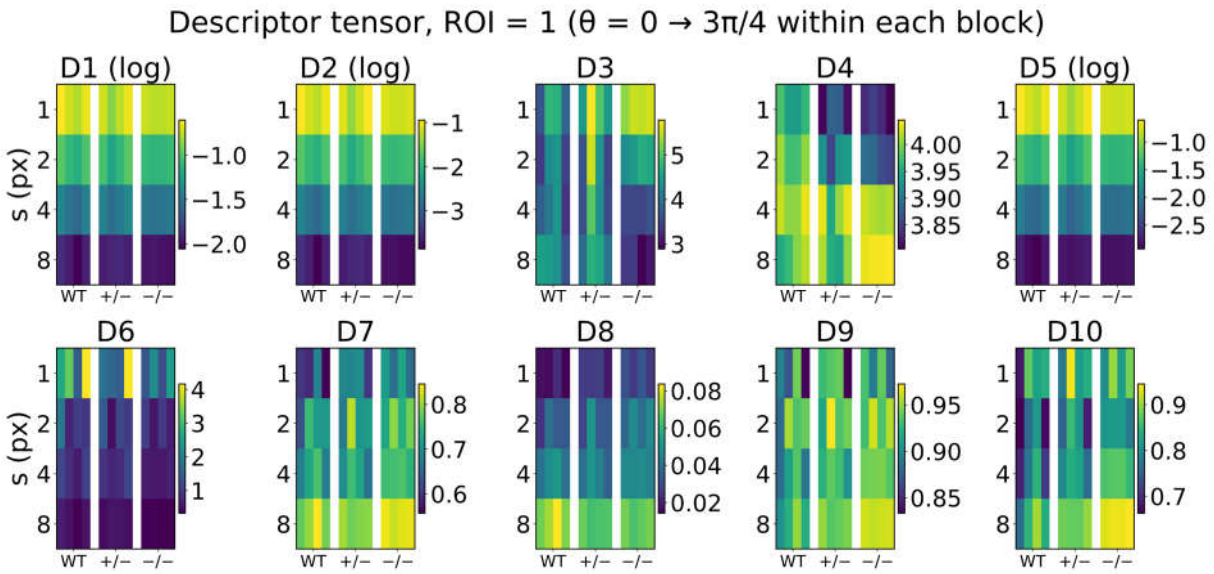


Figure 3. Descriptor tensor $D[m,k,l,1]$ at 10×. Each map has three blocks (WT, *MSTN*+/−, *MSTN*−/−); within a block the four columns are the orientations θ = 0, π/4, π/2, 3π/4 and the rows are the scales s = 1-8 px; channels D1, D2 and D5 are shown on a $\log_{10}$ scale.

Table 1

Mean descriptor channels over the four orientations at s = 2 px, ROI = 1, 10× panels

Channel	*WT*	*MSTN+/−*	*MSTN−/−*
D1 mean |∂G|	0.089	0.085	0.080
D2 mean $(\partial G)^2$	0.015	0.015	0.014
D3 kurtosis	3.88	4.27	4.52
D4 entropy (bits)	3.99	3.91	3.87
D5 mean $\|\partial^2 G\|$	0.045	0.041	0.040
D6 GLCM contrast	1.14	1.01	0.79
D7 GLCM homogeneity	0.701	0.730	0.763
D8 GLCM energy	0.033	0.037	0.043
D9 GLCM correlation	0.928	0.941	0.946
D10 autocorrelation	0.727	0.776	0.806

Luminance standardised to zero mean and unit variance; ROI = 1 contains 63 433-64 578 px.

Anisotropy and texture axis. All nine sections were significantly more anisotropic than their isotropic surrogates (95th percentile of the null A = 0.016-0.026 at s = 2 px; P = 0.005 in 34 of 36 scale-panel combinations and $P \leq 0.035$ in the remaining two). The magnitude of the anisotropy, however, separated the genotypes clearly (Figure 4, Table 2). In WT muscle A was 0.33-0.37 at s = 2 px and reached 0.47 at coarser scales, with a

stable axis $\psi \approx 76$-$82°$ that follows the elongated fibre profiles and the perimysial septa running nearly vertically in the field (Figure 1). *MSTN*+/− muscle was equally or more anisotropic (A up to 0.50 at 10× and 0.56 at 40×, s = 1 px), with an oblique axis of 50-58°, reflecting the regularly aligned, elongated fibre profiles visible in the heterozygous sections. In contrast, the *MSTN*−/− muscle was the most isotropic at every magnification: at s = 2 px A = 0.107 (95% CI 0.050-0.177), 0.059 (0.016-0.176) and 0.138 (0.044-0.266) at 10×, 20× and 40×, and its bootstrap interval did not overlap those of the other genotypes at 10× and 20×. Its texture axis was poorly determined (CI width 35-110°), as expected for an almost isotropic pattern.

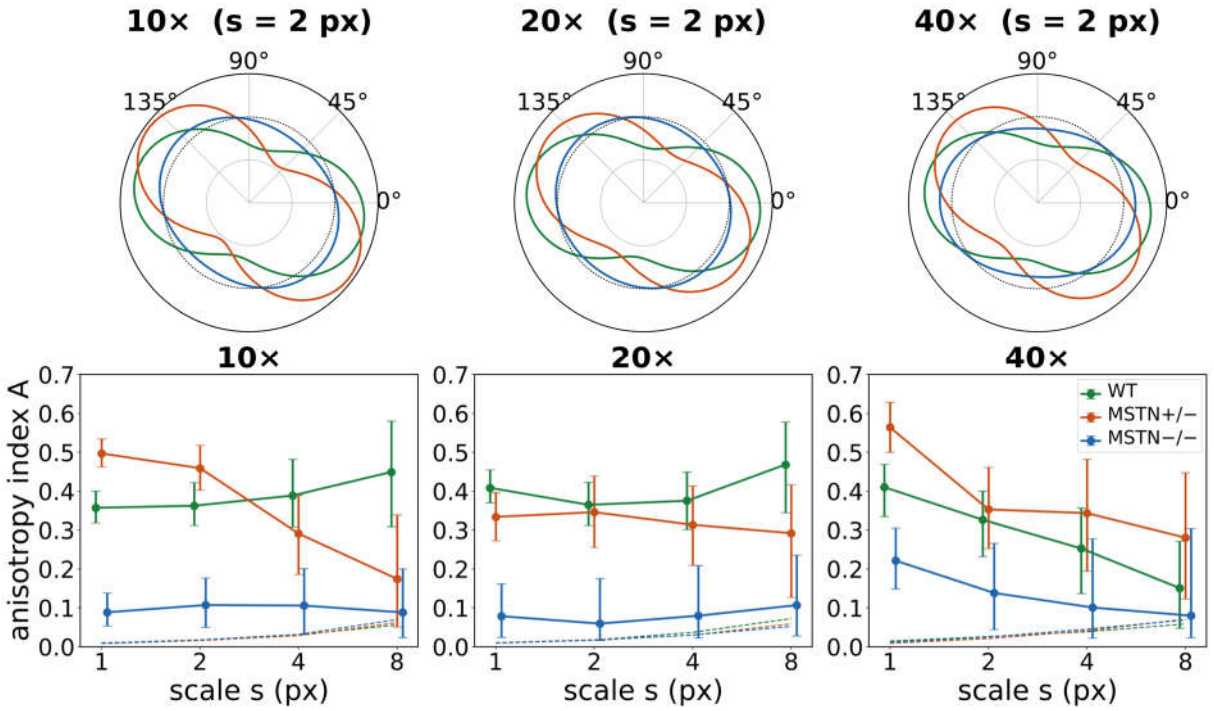


Figure 4. Top: normalised directional energy profiles $1 + A \cos 2(\theta - \varphi)$ at s = 2 px for the three genotypes at each magnification (dotted circle = isotropy). Bottom: anisotropy index A versus scale with block-bootstrap 95% CIs; dashed lines are the 95th percentiles of the isotropic Fourier-phase surrogates.

Table 2

Anisotropy index A, texture axis ψ and structure-tensor field statistics at s = 2 px (ROI = 1)

Mag.	*Genotype*	*A [95% CI]*	*Null 95%*	*ψ (°) [95% CI]*	$\overline{\kappa}$	*R*
10×	WT	0.363 [0.312, 0.422]	0.016	76.2 [71.3, 80.8]	0.41	0.36
10×	MSTN+/−	0.459 [0.402, 0.518]	0.016	53.5 [50.0, 57.0]	0.47	0.45
10×	MSTN−/−	0.107 [0.050, 0.177]	0.018	52.3 [36.4, 71.0]	0.19	0.10
20×	WT	0.365 [0.312, 0.423]	0.017	82.3 [77.3, 86.5]	0.40	0.36
20×	MSTN+/−	0.346 [0.256, 0.439]	0.018	57.9 [51.4, 64.6]	0.39	0.33
20×	MSTN−/−	0.059 [0.016, 0.176]	0.017	50.6 [−0.7, 109.6]	0.30	0.06
40×	WT	0.326 [0.232, 0.400]	0.026	79.6 [71.1, 88.0]	0.40	0.32
40×	MSTN+/−	0.353 [0.253, 0.461]	0.021	50.1 [41.1, 60.1]	0.49	0.35
40×	MSTN−/−	0.138 [0.044, 0.266]	0.025	86.1 [53.9, 117.1]	0.43	0.14

Null 95%: 95th percentile of A for 200 isotropic Fourier-phase surrogates. $\overline{\kappa}$: mean local coherence; R: energy-weighted resultant of local axes of the structure-tensor field (s = 2 px, ρ = 16 px).

Independent structure-tensor field. The windowed structure-tensor field (Figure 5) explains why the knockout appears isotropic. The mean local coherence $\overline{\kappa}$ of *MSTN*−/− muscle was lower at 10× (0.19 vs 0.41 and 0.47) but similar at 40× (0.43), whereas the resultant R of the local axes was the lowest at every magnification (0.06-0.14 vs 0.32-0.45; Table 2). At the scale of a few fibres, the knockout tissue is therefore still locally oriented, but the local axes point in all directions, so they cancel when pooled, as described by the factorisation of A into local coherence and alignment of local axes (Ţălu, 2027b). This is the expected signature of polygonal, tightly packed fibres without a

common elongation direction, and it agrees with the axis ψ obtained independently from the tensor for WT (76.2° vs 76.4°) and *MSTN*+/− (53.5° vs 53.0°).

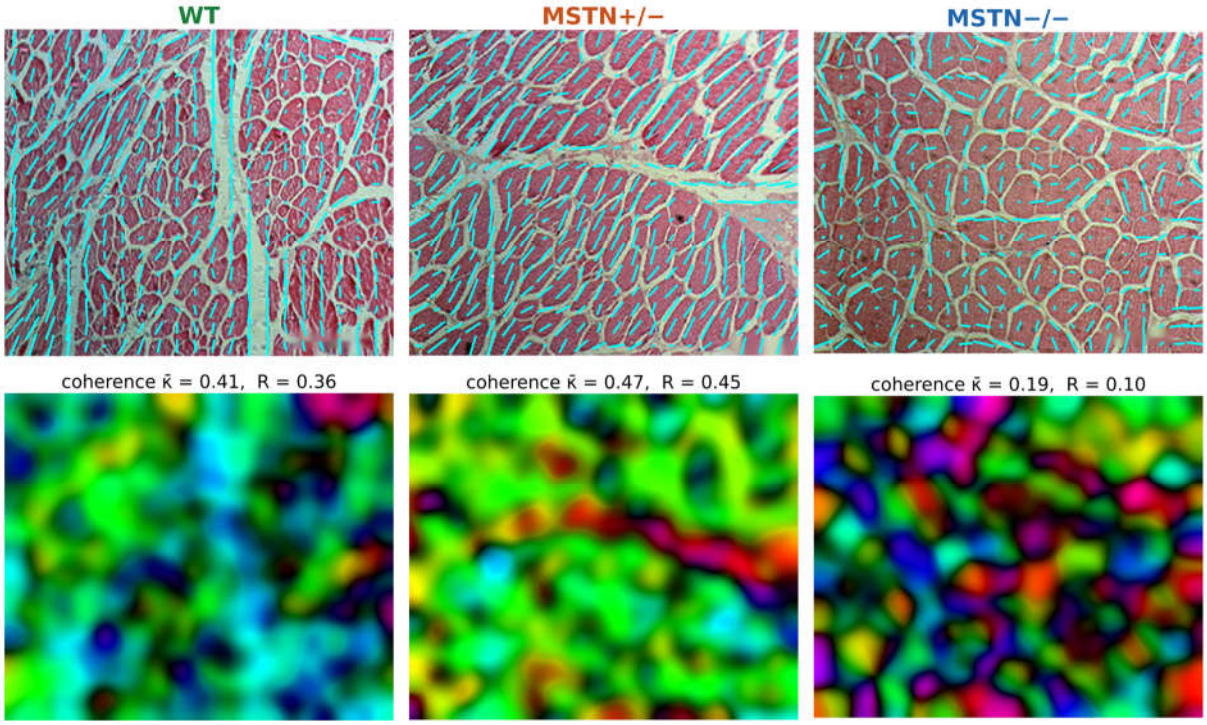


Figure 5. Structure-tensor field at 10×. Top: local texture axes (cyan sticks, length ∝ coherence) over the H&E image. Bottom: colour-coded axis (hue, 0-180°) and coherence (brightness). $\bar{\kappa}$ is the mean coherence and *R* the resultant of the local axes; the *MSTN*−/− field is a mosaic of locally oriented but mutually incoherent domains.

Regional analysis (ROI = 4) and scale. The four-quadrant decomposition (Figure 6, Table 3) showed homogeneous values of *A* in WT (0.34-0.43) and *MSTN*+/− (0.41-0.51), with quadrant axes within ±18° of the global axis. In *MSTN*−/− muscle the quadrant anisotropies were low (0.07-0.22) and the quadrant axes alternated between about 40° and 80-88°. The pooling inequality was satisfied in all nine panels; the ratio of global to energy-weighted mean quadrant anisotropy was 0.95-1.00 for WT and *MSTN*+/− but 0.43-0.76 for *MSTN*−/−, quantifying the loss of anisotropy caused by mutually misaligned regions. The energy curve s^2 tr $J(s)$ reached its maximum at the finest scale in eight of nine panels (an interior maximum, $s^* = 3.5$ px, appeared only for WT at 40×), indicating that most gradient energy lies in the intrafibre striation and fine septa rather than at the fibre scale; for this reason the comparison of genotypes is based on fixed scales rather than on s^*.

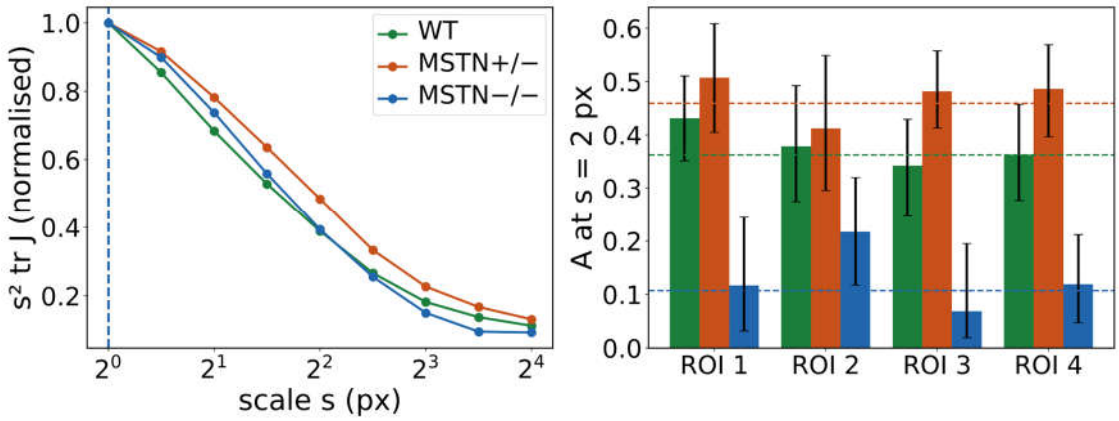


Figure 6. Left: normalised scale-energy curves s^2 tr $J(s)$ at 10× (dashed lines: s^*). Right: anisotropy index *A* in the four quadrants (ROI = 4) at s = 2 px, with block-bootstrap 95% CIs; horizontal dashed lines are the ROI = 1 values.

Table 3

Anisotropy A and axis ψ in the four quadrants (ROI = 4) at s = 2 px, 10× panels

Genotype	*ROI 1*	*ROI 2*	*ROI 3*	*ROI 4*	*A (ROI = 1)*	$\Sigma E_r A_r / \Sigma E_r$
WT	0.431 (62.8°)	0.379 (83.3°)	0.342 (75.0°)	0.363 (83.2°)	0.363	0.380
MSTN+/−	0.507 (46.8°)	0.413 (52.5°)	0.481 (57.1°)	0.487 (61.0°)	0.459	0.467
MSTN−/−	0.117 (87.5°)	0.217 (40.9°)	0.069 (77.4°)	0.119 (40.5°)	0.107	0.140

Quadrants numbered as in Figure 1. The last two columns verify the pooling inequality $A(\cup r) \leq \Sigma E_r A_r / \Sigma E_r$.

Channel redundancy. The Spearman matrix (Figure 7) shows that D1, D2 and D5 are practically redundant (ρ ≥ 0.99), as in human, fish and guppy muscle (Țălu, 2026c, 2027a), and strongly coupled to the GLCM contrast D6 (ρ = 0.88-0.89) and, inversely, to the homogeneity D7 and energy D8 (ρ = −0.78 to −0.89). The kurtosis D3 and entropy D4 form a second, negatively related pair (ρ = −0.84), while GLCM correlation D9 and autocorrelation D10 are nearly independent of the gradient group ($|\rho| \leq 0.23$). A reduced descriptor set of D2, D3, D6, D9 and D10 would therefore retain almost all of the information for this type of tissue.

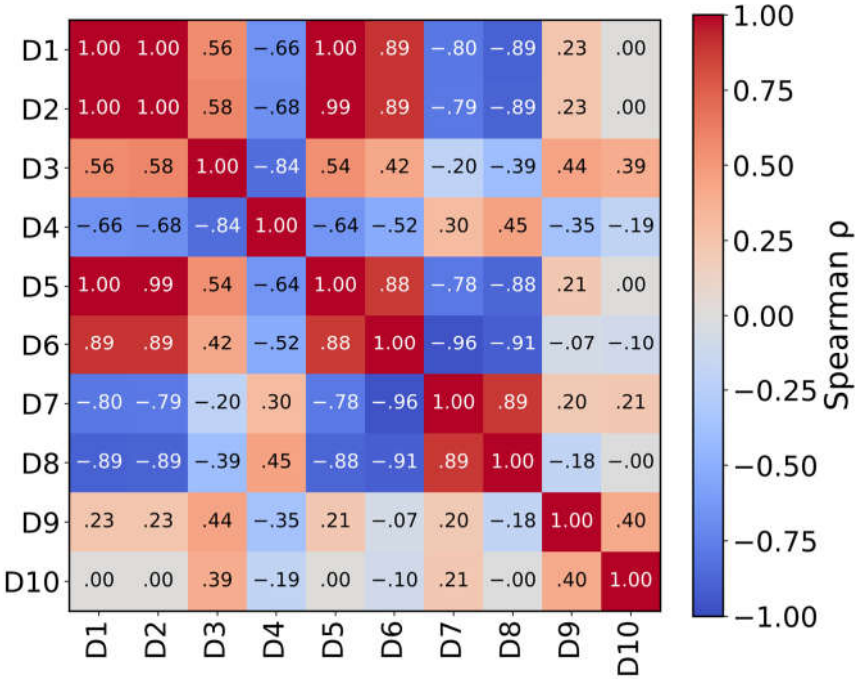


Figure 7. Spearman correlation matrix between the ten descriptor channels computed over all scale × orientation × quadrant entries of the three genotypes (10×).

Agreement with fibre morphometry. The segmentation (Figure 8, Table 4) confirmed the phenotype described by Zheng et al. (2022). At 10× the median fibre area increased from 159 px² in WT to 428 px² in *MSTN*+/− and 553 px² in *MSTN*−/−, the fibre area fraction increased from 0.60 to 0.72, and the *MSTN*−/− fibres were the roundest (median circularity 0.81 vs 0.74 and 0.71). The lower coefficient of variation of area in the edited animals (0.60-0.61 vs 2.06) partly reflects the fragmentation of small WT fibres separated by thin septa. Most importantly, the tensor anisotropy A at s = 2 px was strongly rank-correlated with the orientational order of the segmented fibre profiles over the nine panels (ρ = 0.78, P = 0.013), showing that A is a pixel-level, segmentation-free proxy of fibre alignment and packing.

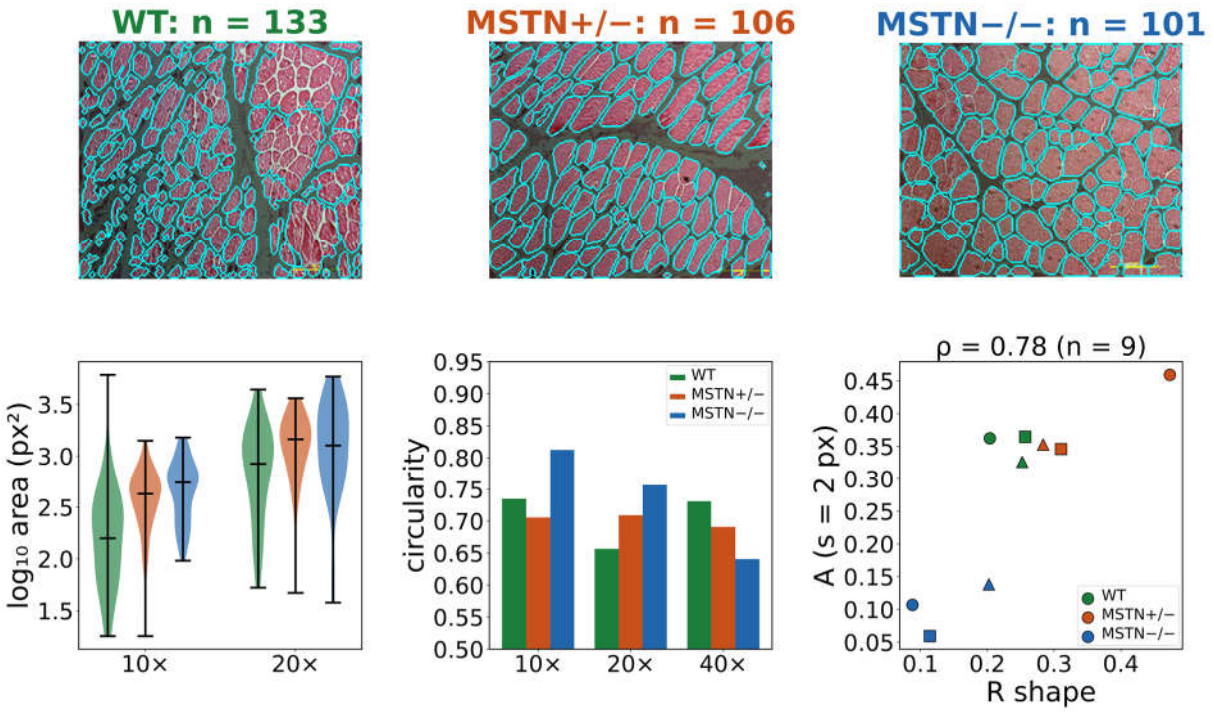


Figure 8. Fibre morphometry. Top: watershed segmentation of the 10× panels (cyan contours; *n* = number of fibre profiles). Bottom left: distribution of fibre areas at 10× and 20× (log scale; bars = median and range). Bottom centre: median circularity. Bottom right: tensor anisotropy *A* (*s* = 2 px) versus fibre-shape orientation order *R*shape for the nine panels (circles 10×, squares 20×, triangles 40×).

Table 4

Fibre morphometry from the segmented H&E panels

Mag.	*Genotype*	*n fibres*	*Median area (px²) [IQR]*	*Density (/10⁴ px²)*	*Fibre fraction*	*Circularity*	*R shape*
10×	WT	133	159 [75-344]	17.5	0.60	0.74	0.20
10×	MSTN+/−	106	428 [253-564]	13.9	0.59	0.71	0.47
10×	MSTN−/−	101	553 [271-687]	13.0	0.72	0.81	0.09
20×	WT	44	843 [349-1498]	5.7	0.61	0.66	0.26
20×	MSTN+/−	34	1458 [812-1914]	4.4	0.63	0.71	0.31
20×	MSTN−/−	32	1286 [718-2550]	4.1	0.73	0.76	0.11

Areas and densities in image pixels; genotypes are comparable within a magnification. IQR: interquartile range.

Robustness to magnification. A principal component analysis of the 160-element tensors of the nine panels (Figure 9, left) shows that the first component (38% of variance) mainly orders the panels by magnification, i.e. by the physical scale sampled by a pixel; genotype differences appear within each magnification. When *A* is compared at approximately the same physical scale (10× with *s* = 4 px, 20× with *s* = 2 px, 40× with *s* = 1 px; Figure 9, right), the *MSTN*−/− muscle remains the most isotropic (0.11, 0.06, 0.22) compared with WT (0.39, 0.37, 0.41). The anisotropy index is therefore the most transferable descriptor across magnifications, whereas raw gradient channels must be compared within the same optical setup.

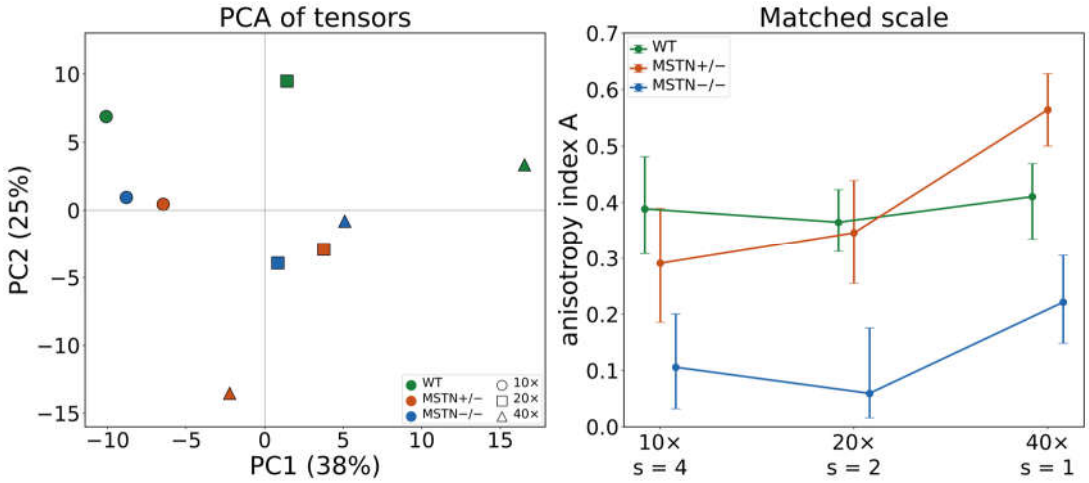


Figure 9. Left: principal component analysis of the standardised descriptor tensors (colour = genotype, symbol = magnification). Right: anisotropy index *A* compared at an approximately matched physical scale, with block-bootstrap 95% CIs.

Replication on an independent study. The second dataset (Figure 10, Table 5) did not reproduce the anisotropy pattern. In the *gluteus maximus* of Lv et al. (2016), the WT section was almost isotropic (A = 0.029, 95% CI 0.008-0.071 at s = 1.19 µm; field resultant R = 0.035) with an undetermined axis, whereas the *MSTN*+/− section was clearly anisotropic (A = 0.214, 0.159-0.275; ψ = 61.8°; R = 0.214). In the tongue, where longitudinal fibre bundles dominate the field, both genotypes were strongly and equally anisotropic (A = 0.311 and 0.323, $\psi \approx$ 84-96°). The geometric meaning of A was nevertheless confirmed: the nearly isotropic WT *gluteus* had the most disordered fibre profiles (Rshape = 0.048 vs 0.148 for *MSTN*+/−), in line with the rank correlation found in the discovery set. Anisotropy therefore describes how fibres were cut and packed in a given field, which differs between laboratories and sections, and is not by itself a marker of genotype.

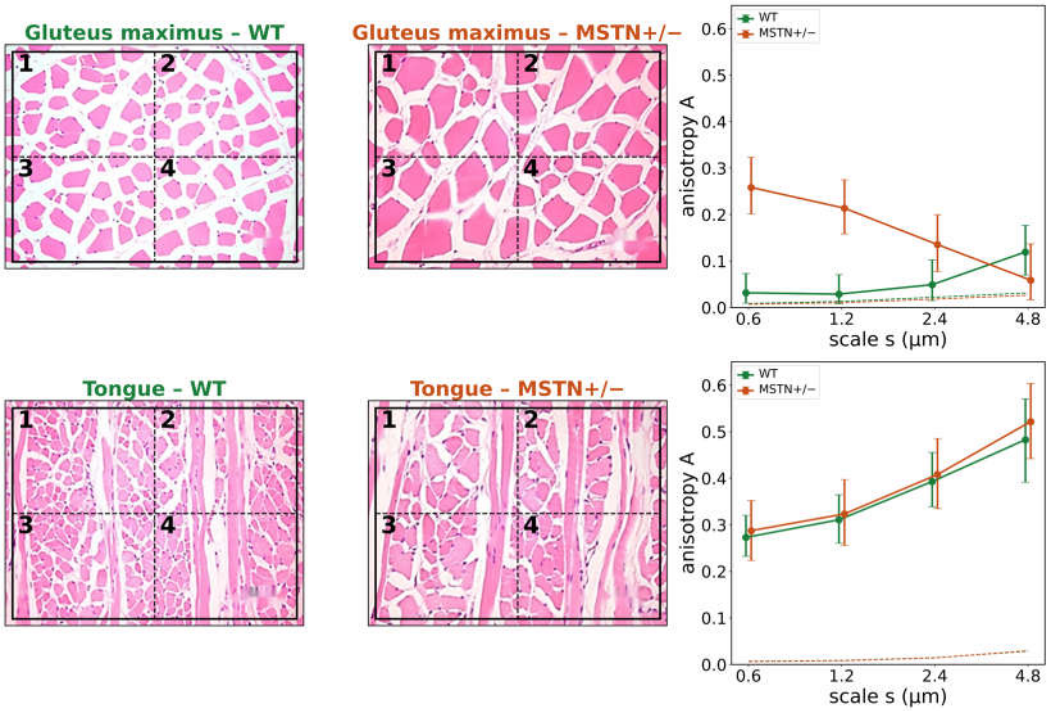


Figure 10. Replication set (Lv et al., 2016, Figure 5A, CC BY 4.0). Left and centre: H&E sections of *gluteus maximus* (top) and tongue (bottom) of WT and *MSTN*+/− rabbits with ROI = 1 (solid frame) and the four quadrants (dashed); scale bars inpainted. Right: anisotropy index A versus physical scale with block-bootstrap 95% CIs; dashed lines are the 95th percentiles of the isotropic surrogates.

Table 5

Descriptor-tensor and morphometric results for the replication set (Lv et al., 2016), s = 2 px = 1.19 µm, ROI = 1

Quantity	*Gluteus WT*	*Gluteus MSTN+/−*	*Tongue WT*	*Tongue MSTN+/−*
A [95% CI]	0.029 [0.008, 0.071]	0.214 [0.159, 0.275]	0.311 [0.261, 0.365]	0.323 [0.256, 0.397]
Null 95%	0.013	0.010	0.009	0.008
ψ (°) [95% CI]	1.3 [−59, 61]	61.8 [53.8, 69.8]	95.6 [92.8, 98.8]	83.7 [80.0, 87.3]
$\overline{\kappa}$ / R (field)	0.26 / 0.04	0.44 / 0.21	0.40 / 0.31	0.47 / 0.32
D3 kurtosis	7.11	7.70	5.47	7.56
D6 GLCM contrast [95% CI]	1.19 [1.12, 1.26]	1.12 [1.04, 1.19]	1.17 [1.11, 1.24]	1.00 [0.95, 1.05]
D7 GLCM homogeneity	0.795	0.798	0.732	0.771
Fibres (n)	117	67	–	–
Mean fibre area (µm²)	438	943	–	–
Median area [IQR] (µm²)	425 [243-578]	830 [435-1384]	–	–
Fibre density (/mm²)	943	540	–	–
Circularity / R shape	0.82 / 0.05	0.74 / 0.15	–	–

Channels D3, D6 and D7 are orientation means at s = 2 px with 6 × 6 block-bootstrap CIs. Morphometry was not applied to the tongue because of the longitudinally cut fibres.

Fibre morphometry of the replication *gluteus* agreed in direction with the original report: the *MSTN*+/− fibres were larger (mean 943 vs 438 µm²; ratio 2.15) than WT, compared with 2011 vs 1319 µm² (ratio 1.53) reported by Lv et al. (2016) for group means. The absolute areas are smaller than those reported, which suggests that the printed scale bar, tissue shrinkage or field selection differ from the original measurements. Notably, the fibre density of the two representative fields (943 vs 540 /mm²) is opposite to the group means reported by the authors (211 vs 328 /mm²), a reminder that a single representative field may not reflect group statistics.

Which descriptors replicate? The forest plot of Figure 11 compares the eight edited-versus-WT pairs. The GLCM contrast D6 was lower in the edited muscle in all eight comparisons (−6.1% to −30.4%), with a 95% CI excluding zero in seven; only the replication *gluteus* (−6.1%, CI −14.7 to +2.3%) was inconclusive. The GLCM homogeneity D7 was higher in all eight (+0.5% to +8.8%; CI excluding zero in six), and the derivative kurtosis D3 was higher in seven of eight (+8% to +38%). The entropy D4 changed sign between magnifications and is not a robust marker. Thus, the co-occurrence pair (lower contrast, higher homogeneity) and, to a lesser extent, the kurtosis form a texture signature that is reproduced across two laboratories, two muscles and three magnifications, whereas anisotropy is study-specific. Biologically, this signature corresponds to larger, more uniformly stained fibre interiors and a smaller fraction of fibre-septum transitions per unit area, which is the expected consequence of fibre hypertrophy in *MSTN*-disrupted muscle.

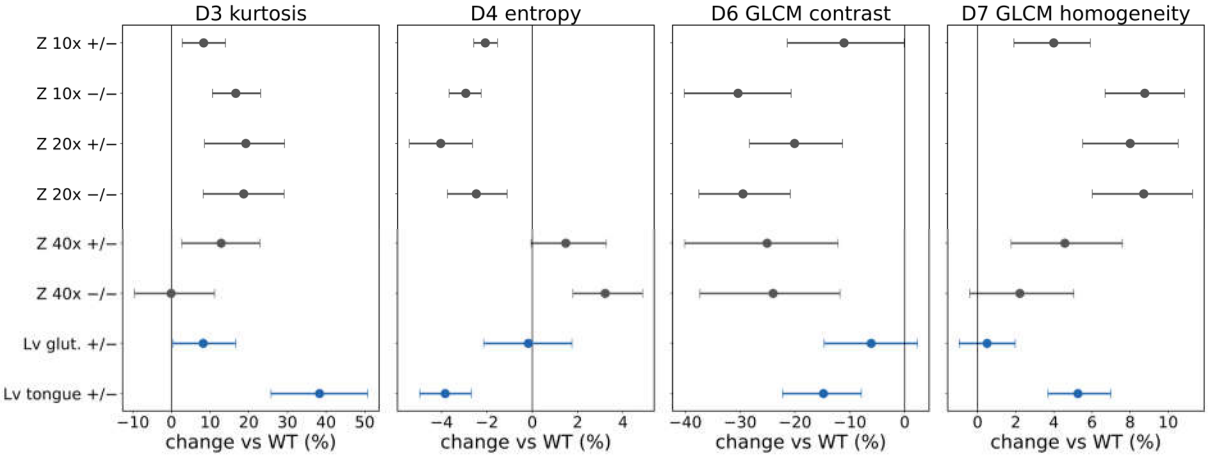


Figure 11. Percentage change of texture channels (orientation mean, s = 2 px) in *MSTN*-edited versus WT muscle for the eight available comparisons (Z: discovery set, Zheng et al., 2022, at 10×, 20× and 40×; Lv: replication set, Lv et al., 2016). Bars are 6 × 6 block-bootstrap 95% CIs; blue symbols mark the independent replication set.

Biological interpretation and limitations. Myostatin limits both the number of fibres formed during development and their postnatal growth (McPherron et al., 1997; Lee, 2004); its disruption therefore produces larger fibres and, in some muscles, more fibres (Lv et al., 2016; Zheng et al., 2022). The descriptor tensor captures this reproducibly as a decrease of co-occurrence contrast and an increase of homogeneity and derivative kurtosis, i.e. smoother fibre interiors with fewer fibre-septum transitions. The loss of global anisotropy found in the *MSTN*−/− muscle of the discovery set was not reproduced in the replication set, where the WT section was the isotropic one; anisotropy depends on the angle of sectioning, the fascicle arrangement within the field and the elongation of the fibre profiles, and should be reported as a geometric covariate rather than as a genotype marker. Several limitations remain. Only one published field per genotype, tissue and magnification was available, so the comparisons describe these images and cannot be generalised to populations without replication across animals. The bootstrap intervals describe spatial variability within each field, not variability between animals, and the discovery comparisons share their WT panels, so the eight comparisons are not independent biological replicates. The co-occurrence channels were also computed at the same displacement in pixels (2 px) at all magnifications, so the consistency of the signature across magnifications and between the two studies has not been verified at a matched physical scale. The images are compressed figure panels; the discovery set could not be calibrated in µm, and the absolute calibration of the replication set gave fibre areas smaller than those reported. Section obliquity and intrafibre clefts affect the finest scales. Replicated, calibrated whole-slide images of WT and edited rabbits would allow formal testing of the genotype effect and the use of the GLCM contrast-homogeneity pair as a quantitative trait in breeding and genome-editing programmes.

Conclusions. The hierarchical descriptor tensor was applied to open-access H&E sections of *MSTN*-edited and wild-type rabbit muscle from two independent CRISPR/Cas9 studies. All sections were significantly anisotropic, and the anisotropy index agreed with the orientational order of segmented fibre profiles (ρ = 0.78), but its relation to genotype was not reproducible between studies: the knockout *gluteus* was the most isotropic in the discovery set, whereas the WT *gluteus* was the most isotropic in the replication set. In contrast, a co-occurrence signature replicated across two laboratories, two muscles and three magnifications: GLCM contrast was lower in all eight edited-versus-WT comparisons (−6% to −30%) and homogeneity higher in all eight, consistent with the larger fibres measured in both studies. The GLCM contrast-homogeneity pair is proposed as a candidate, segmentation-free texture signature of the *MSTN* double-muscle phenotype, pending validation on independent animals, while anisotropy should be treated as a descriptor of section geometry. The workflow is fully reproducible from open-access figures and can complement classical morphometry in rabbit genetics, breeding and genome-editing studies.

Acknowledgements. The author thanks Zheng et al. (2022) and Lv et al. (2016), and the journals Frontiers in Veterinary Science and Scientific Reports, for making the histological images available under open-access licences. This research received no external funding.

Data Availability. No new animal data were generated. The source images are publicly available in Zheng et al. (2022), Figure 7B (https://doi.org/10.3389/fvets.2022.842074), and Lv et al. (2016), Figure 5A (https://doi.org/10.1038/srep25029). The analysis code and the numerical results (descriptor tensors, bootstrap and surrogate statistics, fibre measurements) are available from the author on reasonable request.

Use of generative AI. During the preparation of this manuscript, the author used GPT-6 Astra to assist in the preparation of the graphical abstract and a figure. The author reviewed and edited the AI-assisted visual materials as necessary and take full responsibility for the accuracy, originality, and integrity of all content in the manuscript.

Ethical Statement. This study used only previously published images; no animals were handled by the author. The original experiments were approved by the ethics committees of the source institutions, as stated by Zheng et al. (2022) and Lv et al. (2016).

Conflict of Interest. The author declares that there is no conflict of interest.

References

Bankhead, P., Loughrey, M. B., Fernández, J. A., Dombrowski, Y., McArt, D. G., Dunne, P. D., McQuaid, S., Gray, R. T., Murray, L. J., Coleman, H. G., James, J. A., Salto-Tellez, M., & Hamilton, P. W. (2017). QuPath: Open source software for digital pathology image analysis. *Scientific Reports, 7*, 16878. https://doi.org/10.1038/s41598-017-17204-5

Bigun, J., & Granlund, G. H. (1987). Optimal orientation detection of linear symmetry. In *Proceedings of the First International Conference on Computer Vision* (pp. 433–438). IEEE Computer Society Press.

Conceição, W. S., Țălu, Ș., Matos, R. S., Ramos, G. Q., Zayas, F. G., & da Fonseca Filho, H. D. (2021). Stereometric characterization of *Dinizia excelsa* Ducke wood from Amazon rainforest using atomic force microscopy. *Microscopy Research and Technique, 84*(7), 1431–1441. https://doi.org/10.1002/jemt.23699

Garczyk, Ż., Stach, S., Țălu, Ș., Sobola, D., & Wróbel, Z. (2017). Stereometric parameters of butterfly wings. *Journal of Biomimetics, Biomaterials and Biomedical Engineering, 31*, 1–10. https://doi.org/10.4028/www.scientific.net/JBBBE.31.1

Grobet, L., Martin, L. J., Poncelet, D., Pirottin, D., Brouwers, B., Riquet, J., Schoeberlein, A., Dunner, S., Ménissier, F., Massabanda, J., Fries, R., Hanset, R., & Georges, M. (1997). A deletion in the bovine myostatin gene causes the double-muscled phenotype in cattle. *Nature Genetics, 17*(1), 71–74. https://doi.org/10.1038/ng0997-71

Guo, R., Wan, Y., Xu, D., Cui, L., Deng, M., Zhang, G., Jia, R., Zhou, W., Wang, Z., Deng, K., Huang, M., Wang, F., & Zhang, Y. (2016). Generation and evaluation of Myostatin knock-out rabbits and goats using CRISPR/Cas9 system. *Scientific Reports, 6*, 29855. https://doi.org/10.1038/srep29855

Haralick, R. M., Shanmugam, K., & Dinstein, I. (1973). Textural features for image classification. *IEEE Transactions on Systems, Man, and Cybernetics, SMC-3*(6), 610–621. https://doi.org/10.1109/TSMC.1973.4309314

Kambadur, R., Sharma, M., Smith, T. P. L., & Bass, J. J. (1997). Mutations in myostatin (GDF8) in double-muscled Belgian Blue and Piedmontese cattle. *Genome Research, 7*(9), 910–915. https://doi.org/10.1101/gr.7.9.910

Künsch, H. R. (1989). The jackknife and the bootstrap for general stationary observations. *The Annals of Statistics, 17*(3), 1217–1241. https://doi.org/10.1214/aos/1176347265

Lee, S. J. (2004). Regulation of muscle mass by myostatin. *Annual Review of Cell and Developmental Biology, 20*, 61–86. https://doi.org/10.1146/annurev.cellbio.20.012103.135836

Lindeberg, T. (1998). Feature detection with automatic scale selection. *International Journal of Computer Vision, 30*(2), 79–116. https://doi.org/10.1023/A:1008045108935

Lv, Q., Yuan, L., Deng, J., Chen, M., Wang, Y., Zeng, J., Li, Z., & Lai, L. (2016). Efficient generation of myostatin gene mutated rabbit by CRISPR/Cas9. *Scientific Reports, 6*, 25029. https://doi.org/10.1038/srep25029

McPherron, A. C., Lawler, A. M., & Lee, S. J. (1997). Regulation of skeletal muscle mass in mice by a new TGF-β superfamily member. *Nature, 387*(6628), 83–90. https://doi.org/10.1038/387083a0

Mosher, D. S., Quignon, P., Bustamante, C. D., Sutter, N. B., Mellersh, C. S., Parker, H. G., & Ostrander, E. A. (2007). A mutation in the myostatin gene increases muscle

mass and enhances racing performance in heterozygote dogs. *PLoS Genetics, 3*(5), e79. https://doi.org/10.1371/journal.pgen.0030079

Otsu, N. (1979). A threshold selection method from gray-level histograms. *IEEE Transactions on Systems, Man, and Cybernetics, 9*(1), 62–66. https://doi.org/10.1109/TSMC.1979.4310076

Păpuc, T., & Petrescu-Mag, I. V. (2021). The A locus in domestic rabbit breeds (*Oryctolagus cuniculus*). *Rabbit Genetics, 11*(1), 16–21.

Petrescu-Mag, I. V., Țălu, Ș., & Șahin, D. (2026). Fractal, multifractal and entropy-based approaches in aquaculture: An integrative review. *Aquaculture, Aquarium, Conservation & Legislation, 19*(2), 882–898.

Proorocu, M., & Kovacs, E. (2022). The role of the B locus in the genetics of color in rabbits (*Oryctolagus cuniculus*). *Rabbit Genetics, 12*(1), 28–31.

Proorocu, M., Todoran, C., & Păpuc, T. (2019). Vienna White – a peculiar albinism in rabbits (*Oryctolagus cuniculus*). *Rabbit Genetics, 9*(1), 25–32.

Rezakhaniha, R., Agianniotis, A., Schrauwen, J. T. C., Griffa, A., Sage, D., Bouten, C. V. C., van de Vosse, F. N., Unser, M., & Stergiopulos, N. (2012). Experimental investigation of collagen waviness and orientation in the arterial adventitia using confocal laser scanning microscopy. *Biomechanics and Modeling in Mechanobiology, 11*(3–4), 461–473. https://doi.org/10.1007/s10237-011-0325-z

Schuelke, M., Wagner, K. R., Stolz, L. E., Hübner, C., Riebel, T., Kömen, W., Braun, T., Tobin, J. F., & Lee, S. J. (2004). Myostatin mutation associated with gross muscle hypertrophy in a child. *The New England Journal of Medicine, 350*(26), 2682–2688. https://doi.org/10.1056/NEJMoa040933

Smith, L. R., & Barton, E. R. (2014). SMASH – semi-automatic muscle analysis using segmentation of histology: A MATLAB application. *Skeletal Muscle, 4*, 21. https://doi.org/10.1186/2044-5040-4-21

Telea, A. (2004). An image inpainting technique based on the fast marching method. *Journal of Graphics Tools, 9*(1), 23–34. https://doi.org/10.1080/10867651.2004.10487596

Theiler, J., Eubank, S., Longtin, A., Galdrikian, B., & Farmer, J. D. (1992). Testing for nonlinearity in time series: The method of surrogate data. *Physica D, 58*(1–4), 77–94. https://doi.org/10.1016/0167-2789(92)90102-S

Țălu, Ș. (2012). Texture analysis methods for the characterisation of biological and medical images. *Extreme Life, Biospeology & Astrobiology, 4*(1), 8–12.

Țălu, Ș. (2026a). A multidimensional implementation lattice for translational human and veterinary medicine. *Human & Veterinary Medicine, 18*(1), 9–23.

Țălu, Ș. (2026b). A unified fractal-entropy-manifold framework for multi-modal medical image fusion. *Human & Veterinary Medicine, 18*(1), 40–52.

Țălu, Ș. (2026c). Application of the hierarchical texture-descriptor tensor to histological muscle sections of *Poecilia reticulata*. *Poeciliid Research, 16*(1), 62-74. https://doi.org/10.67784/0096

Țălu, Ș. (2027a). A hierarchical tensor framework for quantitative multiscale and multidirectional biomedical texture characterization. *Human & Veterinary Medicine, 19*(1), 32-53. https://doi.org/10.67784/0095

Țălu, Ș. (2027b). Coherence, alignment and fibre-profile geometry in a hierarchical texture-descriptor tensor: Application to H&E sections of skeletal muscle in wild boar (*Sus scrofa*) and domestic pigs. *Porcine Research, 17*(1). https://doi.org/10.67784/0098

Țălu, Ș. (2027c). Scale and orientation signatures of soil structure in thin sections: A hierarchical descriptor tensor applied to greenhouse soils under conventional, pollution-free and organic management. *Advances in Environmental Sciences, 19*(1). https://doi.org/10.67784/0099

Țălu, Ș., Bramowicz, M., Kulesza, S., Lainović, T., Vilotić, M., & Blažić, L. (2016). Influence of the artificial saliva storage on 3-D surface texture characteristics of contemporary dental nanocomposites. *Journal of Microscopy, 264*(2), 198–206. https://doi.org/10.1111/jmi.12432

Țălu, Ș., Shcherbinin, D. P., Konshina, E. A., & Gladskikh, I. A. (2021). Stereometric and fractal analysis of granulated silver films used in thin-film hybrid structures. *Journal of Microscopy, 281*(1), 46–56. https://doi.org/10.1111/jmi.12948

van der Walt, S., Schönberger, J. L., Nunez-Iglesias, J., Boulogne, F., Warner, J. D., Yager, N., Gouillart, E., Yu, T., & the scikit-image contributors. (2014). scikit-image: Image processing in Python. *PeerJ, 2*, e453. https://doi.org/10.7717/peerj.453

Zheng, Y., Zhang, Y., Wu, L., Riaz, H., Li, Z., Shi, D., Rehman, S. U., Liu, Q., & Cui, K. (2022). Generation of heritable prominent double muscle buttock rabbits via novel site editing of myostatin gene using CRISPR/Cas9 system. *Frontiers in Veterinary Science, 9*, 842074. https://doi.org/10.3389/fvets.2022.842074

Received: 11 September 2026. Accepted: 31 October 2026. Published online: 31 October 2026.
Author:
Ștefan Țălu, The Directorate of Research, Development and Innovation Management (DMCDI), The Technical University of Cluj-Napoca, Constantin Daicoviciu St., no. 15, Cluj-Napoca 400020, Cluj County, Romania, e-mail: stefan.talu@auto.utcluj.ro; stefan.talu1@gmail.com https://orcid.org/0000-0003-1311-7657
This is an open-access article distributed under the terms of the Creative Commons Attribution License (CC BY 4.0), which permits unrestricted use, distribution and reproduction in any medium, provided the original author and source are credited.
How to cite this article:
Țălu, Ș. (2027). Descriptor-tensor texture analysis of myostatin-edited rabbit muscle: A two-study replication. *Rabbit Genetics, 17*(1), 10–24. https://doi.org/10.67784/0097